Electric Field Induced Instability and Pattern Formation in Thin Liquid Films

4 AUTHORS, INCLUDING:

Ashutosh Sharma IITK
Indian Institute of Technology Kanpur
334 PUBLICATIONS **7,407** CITATIONS

SEE PROFILE

Kajari Kargupta
Jadavpur University
60 PUBLICATIONS **1,339** CITATIONS

SEE PROFILE

Electric Field Induced Instability and Pattern Formation in Thin Liquid Films

Ruhi Verma,† Ashutosh Sharma,*,† Kajari Kargupta,‡ and Jaita Bhaumik‡

*Department of Chemical Engineering, Indian Institute of Technology, Kanpur-208 016, India,
and Department of Chemical Engineering, Jadavpur University, Kolkata-700032, India*

Electrostatic field induced instability, morphology, and patterning of a thin liquid film confined between two electrodes with an air gap are studied on the basis of nonlinear 3D simulations, both for spatially homogeneous and heterogeneous fields. In addition to the spinodal flow resulting from the variation of field because of local thickness changes, a heterogeneous imposed field also moves the liquid from the regions of low field to high field, thus allowing a more precise control of pattern. Hexagonal packing of liquid columns is observed for a spatially homogeneous electric field, which is in accord with the e-field experiments on thin polymer films (Schaffer et al. *Nature* **2000**, *403*, 874). For a large liquid volume fraction in the gap, $\varphi \geq 0.75$, the coalescence of columns causes a phase inversion, leading to the formation of air columns or cylindrical holes trapped in the liquid matrix (air-in-liquid dispersion). Locally ordered aligned patterns are formed by imposing a spatial variation of the electrostatic field by using a topographically patterned electrode. For example, multiple rows/lines of liquid columns are formed near the edge of a steplike heterogeneity of the electrode and annular rings of ordered columns or concentric ripples are formed around a heterogeneous circular patch. Simulations predict that the electrode pattern is replicated in the film only when the pattern periodicity, L_p, exceeds the instability length scale on the basis of the minimum interelectrode separation distance, $L_p \geq \lambda_{m-d_{min}}$. Thus, the formation of secondary structures can be suppressed by employing an electrode with deep grooves and stronger field gradients, which produces almost ideal templating. The number density of the electric field induced patterns can be altered by tuning the mean film thickness (or the volume fraction of liquid in the gap), periodicity and depth (amplitude) of the grooves on the top electrode, and the applied voltage. The implications are in electrostatic lithography, pattern replication in soft materials, and the design and interpretation of thin film experiments involving electric fields.

1. Introduction

The stability and pattern formation in thin films are of technological and scientific importance in applications ranging from coating, adhesion, wetting, and membrane morphology to the fabrication of optical and electronic devices, sensors, and biochips. The spinodal instability, morphology, dynamics, and dewetting of thin films engendered by different force fields on uniform substrates have been extensively studied both theoretically[1−17] and experimentally.[18−42] The thin film instability and de- wetting can be triggered by a variety of intermolecular interactions such as the long-range attractive van der Waals force or by the externally applied triggers such as

* To whom correspondence should be addressed. E-mail: ashutos@iitk.ac.in.

† Indian Institute of Technology.

‡ Jadavpur University.

(1) Vrij, A. *Discuss Faraday Soc*. **1966**, *42*, 23.
(2) Ruckenstein, E.; Jain, R. K. *J. Chem. Soc., Faraday Trans. 2* **1974**, *70*, 132.
(3) Williams, M. B.; Davis, S. H. *J. Colloid Interface Sci*. **1982**, *90*, 220.
(4) Sharma, A.; Ruckenstein, E. *Langmuir* **1986**, *2*, 480.
(5) Brochard-Wyart, F.; Daillant, J. *Can. J. Phys*. **1991**, *68*, 1984.
(6) Sharma, A. *Langmuir* **1993**, *9*, 861.
(7) Sharma, A. *Eur. Phys. J. E* **2003**, *12*, 397.
(8) Sharma, A.; Jameel, A. T. *J. Colloid Interface Sci*. **1993**, *161*, 190.
(9) Oron, A.; Davis, S. H.; Bankoff, S. G. *Rev. Mod. Phys.* **1997**, *69*, 931.
(10) Sharma, A.; Khanna, R. *Phys Rev. Lett.* **1998**, *81*, 3463.
(11) Sharma, A.; Khanna, R. *J. Chem. Phys.* **1999**, *110*, 4929.
(12) Oron, A. *Phys. Rev. Lett.* **2000**, *85*, 2108.
(13) Thiele, U.; Velarde, M. G.; Neuffer, K. *Phys. Rev. Lett*. **2001**, *87*, 016104.
(14) Thiele, U.; Neuffer, K.; Pomeau, Y.; Velarde, M. G. *Colloids Surf., A* **2001**, *206*, 135.
(15) Warner, M. R. E.; Craster, R. V.; Matar, O. K. *Phys. Fluids* **2002**, *14*, 4040.
(16) Warner, M. R. E.; Craster, R. V.; Matar, O. K. *J. Colloid Interface Sci.* **2003**, *268*, 448.
(17) Shankar, V.; Sharma, A. *J. Colloid Interface Sci.* **2004**, *274*, 294.
(18) Reiter, G. *Phys. Rev. Lett*. **1992**, *68*, 75.
(19) Sharma, A.; Reiter, G. *J. Colloid Interface Sci*. **1996**, *178*, 383.
(20) Reiter, G.; Khanna, R.; Sharma, A. *Phys. Rev. Lett.* **2000**, *85*, 1432.
(21) Yerushalmi-Rosen, R.; Klein, J.; Fetters, L. *Science* **1994**, *263*, 793.
(22) Gau, H.; Herminghaus, S.; Lenz, P.; Lipowsky, R. *Science* **1999**, *283*, 46.
(23) Herminghaus, S.; Jacobs, K.; Mecke, K.; Bischof, J.; Fery, A.; Ibn-Elhaj, M.; Schlagowski, S. *Science* **1998**, *282*, 916.
(24) Reiter, G.; Sharma, A.; David, M.-O.; Casoli, A.; Khanna, R.; Auroy, P. *Langmuir* **1999**, *15*, 2551.
(25) Boltau, M.; Walheim, S.; Mlynek, J.; Krausch, G.; Steiner, U. *Nature* **1998**, *391*, 877.
(26) Schaffer, E.; Thurn-Albrecht, T.; Russell, T. P.; Steiner, U. *Nature* **2000**, *403*, 874.
(27) Schaffer, E.; Thurn-Albrecht, T.; Russell, T. P.; Steiner, U. *Europhys. Lett*. **2001**, *53*, 518.
(28) Morariu, M. D.; Voivu, N. E.; Schaffer, E.; Lin, Z.; Russell, T. P.; Steiner, U. *Nat. Mater.* **2003**, *2*, 48.
(29) Lin, Z.; Kerle, T. S.; Baker, M.; Hoagland, D. A.; Schaffer, E.; Steiner, U.; Russell, T. P. *J. Chem. Phys.* **2001**, *114*, 2377.
(30) Lin, Z.; Kerle, T.; Russell, T. P.; Schaffer, E.; Steiner, U. *Macromolecules* **2002**, *35*, 3971.
(31) Lin, Z.; Kerle, T.; Russell, T. P. *Macromolecules* **2002**, *35*, 6255.
(32) Harkema, S.; Schaffer, E.; Morariu, M. D.; Steiner, U. *Langmuir* **2003**, *19*, 9714.
(33) Sferrazza, M.; Heppenstall-Butler, M.; Cubitt, R.; Bucknall, D.; Webstar, J.; Jones, R. A. L. *Phys. Rev. Lett*. **1998**, *81*, 5173.
(34) Xie, R.; Karim, A.; Douglas, J. F.; Han, C. C.; Weiss, R. A. *Phys. Rev. Lett*. **1998**, *81*, 1251.
(35) Elbaum, M.; Lipson, S. *Phys. Rev. Lett*. **1994**, *72*, 3562.
(36) Seemann, S.; Herminghaus, S.; Jacobs, K. *Phys. Rev. Lett.* **2001**, *86*, 5534.
(37) Chou, S. Y.; Zhuang, L.; Guo, L. *Appl. Phys. Lett*. **1999**, *75*, 1004.
(38) Chou, S. Y.; Zhuang, L. *J. Vac. Sci. Technol*., *B* **1999**, *17*, 3197.
(39) Pease, L. F., III; Russel, W. B. *Langmuir* **2004**, *20*, 795.
(40) Pease, L. F., III; Russel, W. B. *J. Chem Phys.* **2003**, *118*, 2790.

a temperature gradient or an electric field.[26-32] Intermolecular forces on uniform substrates produce rather disordered patterns although with a well-defined mean length scale. A far greater control and ordering of the resulting structure becomes possible on the substrates with physicochemical heterogeneities[22,43,44] that produce a directed flow of liquid away from the less wettable regions.[43,44] Nonlinear 3D simulations incorporating this chemical potential gradient driven flow identified a set of conditions necessary for an ideal templating of the substrate energy pattern in the thin film structure.[45-51] Indeed, with this strategy, a rich variety of ordered mesoscale patterns could be produced by controlled dewetting of polymers films on heterogeneous substrates.[52-62] The application of an external electric field appears to be another promising and versatile method for the patterning of a thin film by controlling its surface instability.[17,26-32] An applied electric field normal to the film interface causes an interfacial electrostatic pressure, driving the flow in much the same way as the action of van der Waals disjoining pressure on a nonwettable substrate. The interfacial instability caused by a uniform electrical field leads to the formation of a hexagonal pattern under some conditions.[26-32] Experimental studies of the electric field induced instability have reported the morphologies of the polymer−air[26,27] as well as polymer−polymer[28-31] interfaces and the formation of columnar pillar structures. Similar columnar structures were observed even in the absence of an externally applied electric field[32,37,38] for the systems where electric fields are generated naturally from the contact potentials of different interfaces.[63] The application of a laterally varying electric field by using a topologically structured electrode was also reported as a useful means of controlling the lateral dimensions of the microstructures[26,27] and producing features of nanometer sizes. Experiments suggest that patterns down to 100 nm can be replicated by using bilayers of two different polymers.[28]

Theoretically, the problem of electric field induced instability and pattern formation has been studied largely on the basis of linear stability analysis,[17,26,27] which predicts the mean feature spacing at early times but cannot address the problem of precise 3D morphology and its degree of order, even at short times. Recently, Pease and Russel[39,40]
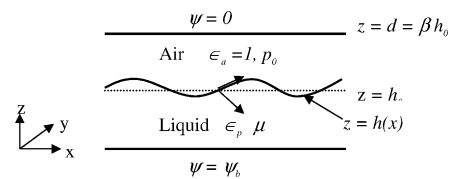
(41) Becker, J.; Grün, G.; Seemann, R.; Mantz, H.; Jacobs, K.; Mecke, K. R.; Blossey, R. *Nat. Mater.* **2003**, *2*, 59.
(42) Onuki, A. *Physica A* **1995**, *217*, 38.
(43) Kargupta, K.; Konnur, R.; Sharma, A. *Langmuir* **2000**, *16*, 10243.
(44) Konnur, R.; Kargupta, K.; Sharma, A. *Phys. Rev. Lett.* **2000**, *84*, 931.
(45) Kargupta, K.; Sharma, A. *Phys. Rev. Lett.* **2001**, *86*, 4536.
(46) Kargupta, K.; Sharma, A. *J. Chem. Phys.* **2002**, *116*, 3042.
(47) Kargupta, K.; Sharma, A. *Langmuir* **2002**, *18*, 1893.
(48) Kargupta, K.; Sharma, A. *J. Colloid Interface Sci.* **2002**, *245*, 99.
(49) Sharma, A.; Konnur, R.; Kargupta, K. *Physica A* **2003**, *318*, 262.
(50) Kargupta, K.; Sharma, A. *Langmuir* **2003**, *19*, 5153.
(51) Thiele, U.; Brusch, L.; Bestehorn, M.; Bär, M. *Eur. Phys. J. E* **2003**, *11*, 255.
(52) Sehgal, A.; Ferreiro, V.; Douglas, J. F.; Amis, E. J.; Karim, A. *Langmuir* **2002**, *18*, 7041.
(53) Suh, K. Y.; Lee, H. H. *J. Chem. Phys.* **2002**, *117*, 6266.
(54) Chabinyc, M. L.; Wong, W. S.; Salleo, A.; et al. *Appl. Phys. Lett.* **2002**, *81*, 4260.
(55) Suh, K. Y.; Lee, H. H. *Adv. Funct. Mater.* **2002**, *12*, 405.
(56) Zhang, Z. X.; Wang, Z.; Xing, R. B.; et al. *Polymer* **2003**, *44*, 3737.
(57) Kim, Y. S.; Lee, H. H. *Adv. Mater.* **2003**, *15*, 332.
(58) Zhang, Z. X.; Wang, Z.; Xing, R. B.; et al. *Surf. Sci.* **2003**, *539*, 129.
(59) Zhang, H. L.; Bucknall, D. G.; Dupuis, A. *Nano Lett* **2004**, *4*, 1513.
(60) Bucknall, D. G. *Prog. Mater. Sci.* **2004**, *49*, 713.
(61) Luo, C. X.; Xing, R. B.; Han, Y. C. *Surf. Sci.* **2004**, *552*, 139.
(62) Luo, C. X.; Xing, R. B.; Zhang, Z. X.; et al. *J. Colloid Interface Sci.* **2004**, *269*, 158.
(63) Herminghaus, S. *Phys. Rev. Lett.* **1999**, *83*, 2539.

Figure 1. Schematic representation of a thin liquid film−air interface confined between two electrodes and subjected to an electric field.

examined the initial stage of instability using an extended linear stability analysis and discussed various limitations on the minimum pattern size. Shankar and Sharma[17] reported the linear and nonlinear equations describing the evolution of the interface between two leaky dielectric liquids. Thus, although the linear analysis is useful in predicting the mean length scale and time scale of instability at early times, none of the theoretical studies have addressed the problem of nonlinear pattern selection and its control by an applied electric field. This issue is of primary concern in the thin film applications of patterning.

Here, on the basis of 3D nonlinear simulations, we study the instability and pattern formation in confined thin dielectric liquid films that are subjected to electrostatic and van der Waals forces. In particular, the following questions are addressed:

(a) What are the conditions that favor a greater order in the evolution of surface instability and the resulting self-organized pattern? For example, should the application of an e-field lead to more nearly hexagonal patterns even though a van der Waals field of the same strength in a thin (<50 nm) film produces a largely disordered dewetting?

(b) What are the different possible morphological transitions that occur as the volume fraction of the liquid is increased or the gap between the dielectric liquid and the top electrode is reduced?

(c) What are the possible thin film patterns that can be induced by using spatially varying electric fields and how can one vary the number density of such patterns?

(d) What are the conditions under which the patterns formed in a thin film replicate the top electrode pattern?

2. Theory

Figure 1 shows a schematic of the thin perfect linear isotropic dielectric liquid film ($0 \leq z \leq h$) and air ($h \leq z \leq d$) interface confined between two parallel rigid electrodes. The system is subjected to a constant voltage, ψ_b. The mean film thickness is $z = h_0$. It is assumed that the material properties of the liquid such as viscosity, μ, and dielectric constants, ϵ_p, are constant.

2.1. Governing Equations. The surface evolution for a thin Newtonian film is derived on the basis of the continuity and Navier−Stokes equations simplified in the long-wave approximation. Indeed, the surface instability of thin films in general is of the long-wave type, which is also known to be the case for the e-field induced instability.[17,26-32] The following thin film equation[3,4,6-16,43-51] describes the spatiotemporal evolution of the interface, $h(x,y,t)$, in the long-wave limit.

$$3\mu(\partial h/\partial t) - \nabla\cdot[h^3\nabla P] = 0 \qquad (1)$$

At the free interface, $z = h(x,y,t)$, the normal stress condition relates the total pressure to the curvature, the intermolecular conjoining pressure, ϕ, and the Maxwell stress tensor due to the electrostatic field:[17,25-27]

$$P = p_0 - \gamma \nabla^2 h + \phi_i + \epsilon_0 \{\epsilon_p (\partial \psi_p/\partial z)^2 - \epsilon_a (\partial \psi_a/\partial z)^2\}/2 \tag{2}$$

where ϕ_i is the excess intermolecular interaction potential per unit volume (conjoining pressure) engendered by the van der Waals interactions and an extremely short-range Born repulsion when contact lines appear at later times. We assume that the lower electrode supporting the film is completely wetting because of van der Waals interactions in the absence of the applied electric field. The short-range repulsion becomes effective between the top electrode and the film surface at later times when the columns span across the air gap and come into "contact" with the top electrode. The subscripts a and p denote the air and polymeric liquid phases, respectively, ϵ_0 is the dielectric permittivity of the vacuum, ϵ_p is the dielectric constant of the liquid, and $\epsilon_a = 1$ is the dielectric constant of air. For a perfect dielectric liquid with a space invariant dielectric constant, ϵ_p, the effect of electric field affects the flow only through the boundary conditions at the interface. The bulk of the fluid in this case is free from net charge. We later use the symbol ϵ_h to denote the amplitude of the top patterned electrode, which is not to be confused with the dielectric constant of the liquid, ϵ_p.

In the long-wave limit, the governing equations for the electric potentials, ψ_p and ψ_a ($\nabla^2 \psi_i = 0$), are

$$\partial^2 \psi_p/\partial z^2 = 0; \; \partial^2 \psi_a/\partial z^2 = 0 \tag{3}$$

The boundary conditions are

$$\psi_p = \psi_b \text{ at } z = 0; \; \psi_a = 0 \text{ at } z = d \; (=\beta h_0)$$

$$\psi_a = \psi_p \text{ and } \epsilon_p(\partial \psi_p/\partial z) = \epsilon_a(\partial \psi_a/\partial z) \text{ at } z = h(x,y,t) \tag{4}$$

The solutions of eqs 3 and 4 are

$$\psi_p = \psi_b\{1 + z/[\epsilon_p d - h(\epsilon_p - 1)]\}$$

$$\psi_a = \psi_b \epsilon_p\{[z - d]/[\epsilon_p d - h(\epsilon_p - 1)]\} \tag{5}$$

which lead to

$$P = p_0 - \gamma \nabla^2 h + \phi_i + \phi_{EL} \tag{6}$$

where

$$\phi_{EL} = -0.5\epsilon_0 \epsilon_p (\epsilon_p - 1)E_p^2 \tag{7}$$

and

$$E_p = \psi_b/[\epsilon_p d - (\epsilon_p - 1)h] \tag{8}$$

where E_p (in V/m) is the electrical field in the liquid and ϕ_{EL} is the resulting conjoining pressure due to the electrostatic interaction. For a specified distance between two electrodes, the electrostatic free energy, $\Delta G_{EL} = -(0.5\epsilon_0 \epsilon_p \psi_b^2/[\epsilon_p d - (\epsilon_p - 1)h])$, and its second derivative, $\partial \phi_{EL}/\partial h$, decrease monotonically with the increase in the mean film thickness (Figure 2a).

The resulting thin film equation is

$$3\mu \partial h/\partial t - \nabla \cdot [h^3 \nabla \phi] + \nabla \cdot [h^3 \nabla(\gamma \nabla^2 h)] = 0 \tag{9}$$

where ϕ is the total interaction potential (conjoining pressure) resulting from the following three components: (i) the pressure due to electrostatic attraction, ϕ_{EL}, (ii) the pressure due to net (repulsive) van der Waals interaction, ϕ_{vdW}, between the lower electrode and the film, and (iii)
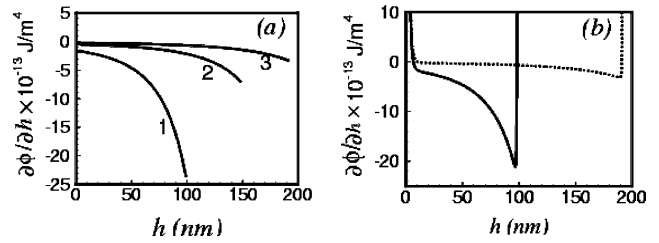

Figure 2. Variation of spinodal parameter, $\partial \phi/\partial h$, with the film thickness for various electrode spacings. (a) For electrostatic attraction, ϕ_{EL}, curves 1, 2, and 3 are for $d = 100$, 150, and 193 nm, respectively. (b) For the total interaction, $\phi_{EL} + \phi_{vdW} + \phi_{Br}$, the solid curve is for $d = 100$ nm and the broken curve is for $d = 193$ nm. The parameters used are the following: $\psi_b = 70$ V, $\epsilon_p = 2.5$, $A = -20 \times 10^{-20}$ J, $\gamma = 38$ mJ/m^2, and $\mu = 1$ Pa s.

the pressure due to extremely short-range Born repulsion, ϕ_{Br}, between the top electrode and the film.

It may be noted that the gradient of potential, $\nabla \phi$, in eq 9 includes the force because of the local film thickness variations, $(\partial \phi/\partial h)\nabla h$, and also the force resulting from the imposed spatial heterogeneity of the electric field, $E_p(x,y)$. The latter can be imposed either by a spatial variation of the applied potential, $\psi_b(x,y)$, or by using a patterned electrode where the interelectrode distance varies as $d(x,y)$. In this paper, we explore the latter option, since it can be translated more easily into practice by the use of a lithographically patterned electrode. The first component of force, $-(\partial \phi/\partial h)\nabla h$, at a given location, engenders the well-known spinodal instability of a spatially homogeneous field by causing a flow from the thinner to thicker regions of the film whenever the spinodal parameter is negative, $(\partial \phi/\partial h) < 0$.[1–17] This condition is always met for the electrostatic field considered here, eq 7. The second force due to the heterogeneity of the electric field, $\nabla \phi_{EL}$, at constant thickness moves the fluid from the low to high regions of electric field,[43–51] for example, from the regions where the electrode spacing (air gap) is higher to those where it is lower. This effect is similar to the movement of a liquid in a thin film from the lower wettability to higher wettability regions on a substrate.[43–51] However, the use of an e-field provides additional and more flexible control strategies for directed movements of a fluid and its patterning compared to wettability control by relatively short-range van der Waals and other intermolecular interactions, which can only be modulated by a change in the material properties.

The total potential is represented as

$$\phi = \phi_{EL} + \phi_{vdW} + \phi_{Br}$$

The last two terms of the above equation are given by

$$\phi_{vdW} + \phi_{Br} = A/6\pi h^3 + 6B_{c1}/(d - h)^7 \tag{10}$$

where A is an effective Hamaker constant ($A = A_{ff} - A_{sf}$, where the subscripts s and f represent the lower solid plate (electrode) and the liquid, respectively). The Hamaker constant is also related to the surface tension by[6–8] $A_{ii} \propto \gamma_i$ and $A_{ij} = (A_{ii}A_{jj})^{1/2}$. The lower electrode is considered to be completely wettable in the absence of an electric field, implying $A_{ff} < A_{sf}$ or $\gamma_s > \gamma_f$. Thus, the film is initially stable on the lower electrode and the instability is initiated by applying an electric field of sufficient strength. When the air gap thickness become very small ($d - h \sim l_0$) and contact lines appear on the top electrode, the fluid is also subjected to a steep repulsion, ϕ_{Br}, which avoids the contact-line singularity and ensures nonpenetration of liquid in the top electrode at contact. The parameter B_{c1}
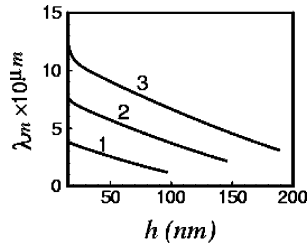
Figure 3. Variation of the dominant instability length scale with film thickness. Curves 1, 2, and 3 are for $d = 100$, 150, and 193 nm, respectively. The parameters used are the following: $\psi_b = 70$ V, $\epsilon_p = 2.5$, $A = -20 \times 10^{-20}$ J, $\gamma = 38$ mJ/m^2, and $\mu = 1$ Pa s.

is evaluated using the condition ϕ (at $h = d - l_0$) = 0, where l_0 is a cutoff thickness (~ 1 nm) where the total conjoining pressure is zero. Note that no van der Waals cutoff is required in our simulations as the film thickness, $h \rightarrow 0$, because we have considered van der Waals repulsion near the bottom electrode (completely wettable bottom surface). It may be noted however that the intermolecular interaction terms in eq 10 have a rather negligible influence compared to the electrostatic term, ϕ_{EL}, but have been retained for completeness.

The spinodal stability of the liquid film depends on the sign of the spinodal parameter, which is the second derivative of the excess free energy per unit area, $\partial^2 \Delta G/\partial h^2 = \phi_h = \partial\phi/\partial h$. The film is spinodally unstable only when $\partial\phi/\partial h < 0$. Figure 2a depicts a monotonically increasing $-\phi_h$, which is also the qualitative variation of ΔG, with increasing film thickness for the electrostatic interaction ($d = 100$, 150, and 193 nm). Variation of the total spinodal parameter, $\partial\phi/\partial h$, is depicted in Figure 2b. When combined with the longer-range electrostatic interactions, the effect of van der Waals interaction (and the Born repulsion) is confined only near the solid surfaces, close to the film rupture or the contact of the free surface with the top electrode. The magnitude of the negative spinodal parameter, $-\partial\phi_{EL}/\partial h$, due to electrostatic attraction is larger than the magnitude of $-\partial\phi_{vdW}/\partial h$ by 2 orders of magnitude for $\psi_b \sim 70$ V. Also, the electrostatic force decays more slowly compared to the van der Waals force. However, a very small threshold value of voltage (~ 0.1 V) is required for the electrostatic field instability to occur, below which the film is stable on the lower electrode because of the repulsive van der Waals interaction.

2.2. Linear Stability Analysis. Linear stability analysis of eq 9 for a homogeneous electric field gives the dominant length scale and time scale of instability. The dimensional evolution eq 9 is linearized using $h = h_0 + \epsilon \exp(\iota(kx + ky) + \omega t)$, where k is the wavenumber, ω is the growth coefficient, and ϵ is the amplitude ($\ll h_0$) of the initial disturbance. The resulting linear dispersion relation is $\omega = -h_0^3 k^2 ((\phi_h)_0 + k^2\gamma)/3\mu$, where $(\phi_h)_0$ denotes $\partial\phi/\partial h$ evaluated at the mean film thickness, h_0. The dominant wavenumber, k_m, of the fastest growing ($\partial\omega/\partial k = 0$) linear mode is given by $k_m = (-(\phi_h)_0/2\gamma)^{1/2}$. The dominant wavelength ($\lambda_m = 2\pi/k_m$) is thus[1-6]

$$\lambda_m = 2\pi(-(\phi_h)_0/2\gamma)^{-1/2}$$

For electrostatic interactions that are initially dominant, $\phi \sim \phi_{EL}$, this gives[17,25-27]

$$\lambda_m = 2\pi\{2\gamma\psi_b/(\epsilon_0\epsilon_p(\epsilon_p - 1)^2)\}^{1/2} E_p^{-3/2} \quad (11)$$

Figure 3 summarizes the dominant length scales predicted by the linear theory. As expected, an increase in the air

gap, $(d - h)$, reduces the electric field, makes the instability weaker, and thus increases its wavelength.

The maximum growth factor is given by $\omega_m = h_0^3((\phi_h)_0)^2/12\mu\gamma$, and the corresponding linear time scale for the growth of instability is obtained as

$$t_r = (1/\omega_m)\ln(h_0/\epsilon) = 12\mu\gamma[h_0^3((\phi_h)_0)^2]^{-1}\ln(h_0/\epsilon) \quad (12)$$

2.3. Nondimensional Equation. The following scales were used to nondimensionalize the governing equations and the boundary conditions:

$$Z = z/h_0; \quad \Phi = \phi h_0^2/[0.5\epsilon_0\epsilon_p(\epsilon_p - 1)\psi_b^2];$$
$$T = t[0.5\epsilon_0\epsilon_p(\epsilon_p - 1)\psi_b^2]^2/\{3\mu\gamma h_0^3\},$$
$$X = x/\{[\gamma h_0^3/0.5\epsilon_0\epsilon_p(\epsilon_p - 1)\psi_b^2]^{1/2}\};$$
$$Y = y/\{[\gamma h_0^3/0.5\epsilon_0\epsilon_p(\epsilon_p - 1)\psi_b^2]^{1/2}\}$$

A renormalized time, t_N (in units of nm^3), is also defined to remove the influence of mean film thickness:

$$t_N = Th_0^3 = t[0.5\epsilon_0\epsilon_p(\epsilon_p - 1)\psi_b^2]^2/3\mu\gamma\}$$

This is used for comparing results for different thickness films at the same real time.

The nondimensional equation is thus obtained in a compact form as

$$\partial H/\partial T + \nabla\cdot[H^3\nabla(\nabla^2 H)] - \nabla\cdot[H^3\nabla\Phi] = 0 \quad (13)$$

where $H(X,Y,T)$ is the nondimensional thickness of the interface between two fluids, T is nondimensional time, X and Y are nondimensional spatial coordinates, and Φ is the total nondimensional conjoining pressure.

2.4. Numerical Methods. The above nondimensional equation was numerically solved for two-dimensional and three-dimensional morphologies. A central difference scheme with the Everett method interpolation was used for spatial discretization of the equation. The time integration was done using Gear's method, which is especially suitable for stiff equations. The simulation domain in most cases was taken to be $4\lambda_m \times 4\lambda_m$ for 3D simulations. Periodic boundary conditions were employed over the simulation domain, and the initial condition was a volume preserving random disturbance of small amplitude. Numerical accuracy and convergence was checked by varying the number of grid points. In most cases, 900 grids in an area of λ_m^2 were found to be satisfactory.

3. Results and Discussions

3.1. Morphologies in Homogeneous Electric Field and Phase Inversion: Columns and Holes. For the purpose of illustrating the behavior of liquid films under an external field, we consider a typical polymer film on a completely wettable substrate. The parameters used are the following: $\psi_b = 70$ V, $\epsilon_p = 2.5$, $A = -20 \times 10^{-20}$ J, $\gamma = 38$ mJ/m^2, and $\mu = 1$ Pa s.

Figures 4–6 depict the morphological evolution of the film–air interface for different thicknesses (volume fractions) of the liquid film and a fixed distance (100 nm) between the electrodes. A large number of simulations (not all of which are shown here) predict that the morphological transitions during the evolution of the air–liquid interface crucially depend on the ratio of the thickness of the air gap to the thickness of the liquid layer, $\xi = (d - h_0)/h_0$. Initial random perturbations first reorganize themselves on the length scale predicted by the linear theory. Further evolution always first forms the columnar
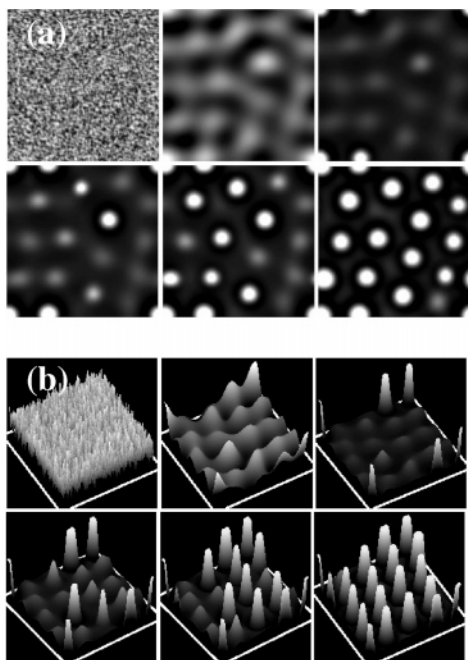
Figure 4. (a) Spatiotemporal evolution of a 25 nm (h_0) thick film on a $4\lambda_m \times 4\lambda_m$ domain, where λ_m is the characteristic length scale from the linear theory. The distance between two electrodes is 100 nm (d). Continuous shading between the maximum and minimum thickness in each image is used. Black represents the minimum thickness, and white represents the maximum thickness in all the figures. The nondimensional times of images 1−6 are $T = 13$, 792 867, 1 108 590, 1 206 421, 1 260 920, and 1 377 584, respectively. (b) 3D surface profiles of the images in part a. The parameters used are the following: $\psi_b = 70$ V, $\epsilon_p = 2.5$, $A = -20 \times 10^{-20}$ J, $\gamma = 38$ mJ/m², and $\mu = 1$ Pa s.
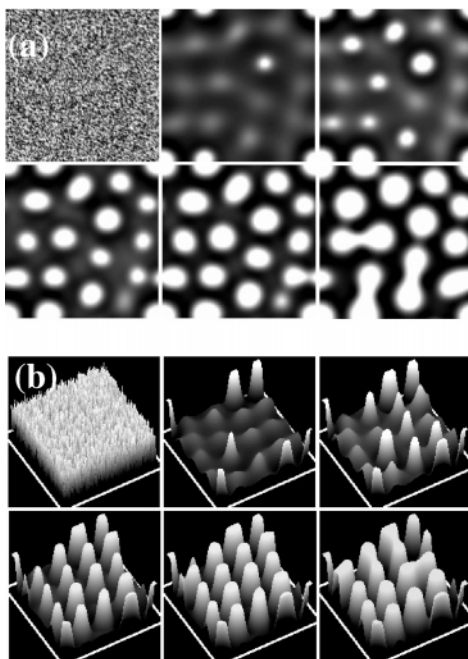

Figure 5. (a) Spatiotemporal evolution of a 50 nm thick film. The distance between two electrodes is 100 nm. The non-dimensional times of images 1−6 are $T = 0$, 5007, 5437, 5858, 6386, and 9567, respectively. (b) 3D surface profiles of the images in part a. Black represents the minimum thickness, and white represents the maximum thickness.

structures (dispersion of liquid in air) that rise and eventually attach to the top electrode. A hexagonal arrangement of columns becomes increasingly more
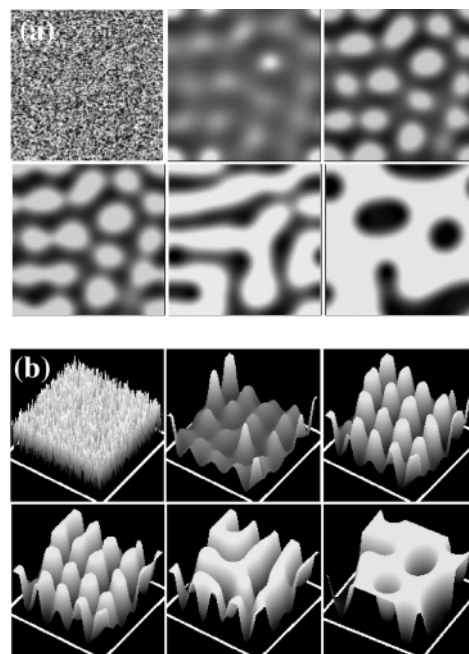

Figure 6. (a) Spatiotemporal evolution of a 75 nm thick film. The distance between two electrodes is 100 nm. The non-dimensional times of images 1−6 are $T = 0$, 92, 113, 125, 200, and 540, respectively. (b) 3D surface profiles of the images in part a. Black represents the minimum thickness, and white represents the maximum thickness.
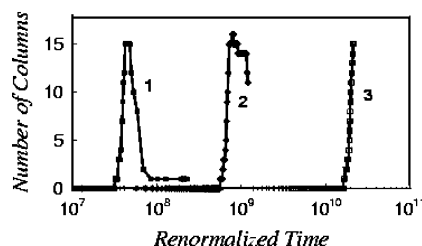

Figure 7. Kinetics of column growth for different initial film thicknesses. Curves 1, 2, and 3 correspond to 75, 50, and 25 nm thick film ($d = 100$ nm in each case). A renormalized time, t_N, in units of nm³ (defined as $t_N = Th_0^3$) is used to remove the influence of the film thickness from the definition of the nondimensional time, T.

prominent as ξ increases, or in other words, liquid is greatly depleted by the formation of columns. For a large value of ξ (>3; Figure 4), isolated quasi-stable columns arranged on hexagonal arrays are formed and persist for long times. The simulated pattern closely resembles the experimentally obtained columnar microstructure.[26−32] The number density of the columns (16 columns on a $16\lambda_m^2$ domain; Figure 7) indeed matches with the number density predicted by the linear theory. This and other similar simulations not shown here all indicate that the diameters of the quasi-stable columns, which do not show coalescence and ripening over a long time, are close to $\lambda_m/2$. A decrease in ξ (=1; Figure 5), implying an increase in the volume fraction of the liquid, leads to the formation of columns of slightly elliptic cross section showing poorer order. The average column diameter also becomes larger than $\lambda_m/2$, which is also in conformity with a simple mass balance. The columns start to coalesce together more rapidly (image 6 of Figure 5a and b). For a still smaller value of ξ (=0.333; Figure 6), the columns formed initially coalesce very rapidly with each other and soon form continuous liquid channels (image 5 of Figure 6a and b). Thus, the greater initial volume fraction of the liquid engenders larger diameter columns and faster intercolumn coalescence and
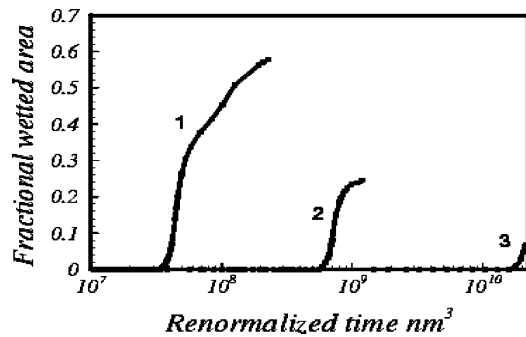
Figure 8. Kinetics of the increase in wetted area of the top electrode by liquid. Curves 1, 2, and 3 correspond to mean film thicknesses of 75 nm ($\xi = 0.33$), 50 nm ($\xi = 1$), and 25 nm ($\xi = 3$), respectively.

ripening of the structure (Figure 7). Further evolution leads to the formation of channels of air, which disintegrate to form circular cylindrical holes entrapped within a continuous liquid matrix (image 6 of Figure 6a and b). Finally, smaller holes begin to disappear due to ripening, and at very large times, a single circular hole remains (not shown). This represents the global minimum of energy for such a system. Thus, a phase inversion from the initial liquid-in-air dispersion to an air-in-liquid dispersion occurs at a higher volume fraction of liquid in the gap. Coalescence of columns and phase inversion sharply increases the fractional wetting of the top electrode by liquid as ξ is decreased from 3 to 0.33 (Figure 8). Figure 8 depicts the increase in the fractional wetted area of the top electrode from 0.07 to 0.58 as ξ decreases from 3 to 0.33; that is, the volume fraction of liquid, φ, increases from 0.25 to 0.75. Interestingly, it was observed on the basis of a large number of simulations that the morphology transition depends crucially on the ratio ξ and not individually on the variation of h_0 and d. The initial volume fraction of the liquid in the gap thus determines whether a quasi-stable liquid-in-air dispersion (columns of liquid in air) or an air-in-liquid dispersion (cylindrical holes or columns of air in liquid) will result due to the electrostatic instability of a thin liquid film. This transition is akin to that observed in dewetting of a thin (<50 nm) film under the influence of an attractive intermolecular force (for example, a van der Waals force), where relatively thick films break up by the formation of holes (air-in-liquid dispersion) but thinner films dewet directly by the formation of droplets (liquid-in-air dispersion).[10−13]

The instability wavelength found from the simulations is indeed long-wave ($\lambda_m \gg h$) and in accord with the linear theory predictions from eq 11. However, it may be noted this long-wave approximation leading to eq 1 becomes quantitatively inadequate at the last stages of column formation and near the column edges where local slopes become large. Since much of the evolution occurs during the slow initial phases of growth before the final rapid formation of contact lines, the long-wave analysis is expected to be largely adequate.

3.2. Control of Patterns by a Heterogeneous Electric Field. In this section, we describe the control of pattern formation to produce ordered patterns in the presence of a spatially heterogeneous electric field. The heterogeneity in electric field is introduced by local variations of spacing between the two electrodes, which can be achieved by lithographic techniques. Four different cases of patterned electrodes are considered: (i) straight edge, in which the distance between the two electrodes changes across an edge, producing a step variation of electric field across the edge; (ii) elevated circular patch
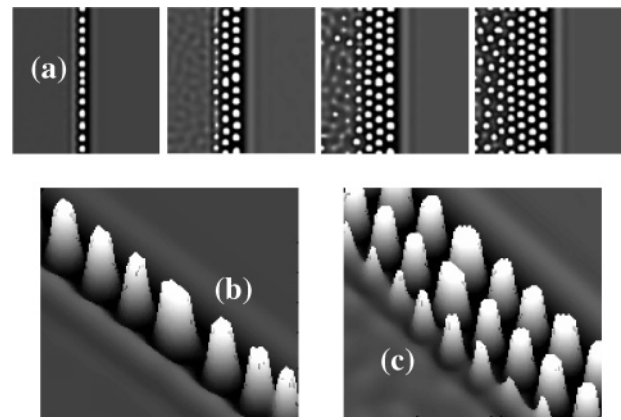

Figure 9. (a) Spatiotemporal evolution of a 50 nm (h_0) thick film. The distance between the two electrodes is 150 nm (d_h) and 193 nm (d) at the left and right sections of the images, respectively. The nondimensional times of images 1−4 are T = 42 940, 93 211, 125 498, and 144 654, respectively. (b and c) Magnified 3D surface profiles of images 1 and 2 in part a, respectively. Black represents the minimum thickness, and white represents the maximum thickness.
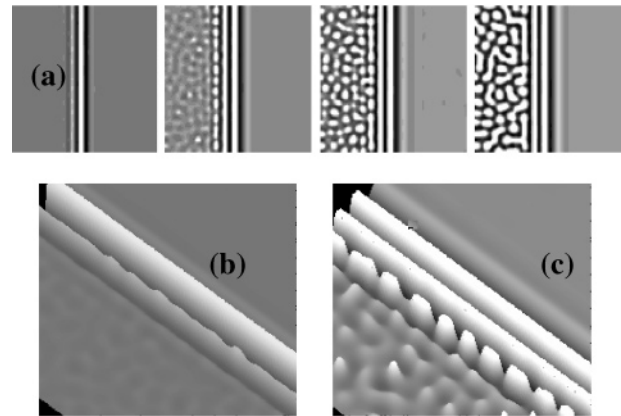

Figure 10. (a) Spatiotemporal evolution of a 93 nm thick film. The distances between two electrodes are 150 and 193 nm at the left and right sections of the images, respectively. The nondimensional times of images 1−4 are T = 287.2, 558.6, 743.2, and 1013, respectively. (b and c) Magnified 3D surface profiles of images 1 and 2 in part a, respectively.

on the top electrode, where the electric field is stronger compared to that applied to its surroundings; (iii) periodic sinusoidal variation, where the electric field is higher at the protrusions of the top electrode and lower at the crests; (iv) block patterned electrode, which consists of arrays of protrusions of rectangular cross section resulting in the minimum separation distance and stronger electric field at these positions compared to the surrounding channels.

3.2.1. Heterogeneity I: Straight Edge. Figures 9a and 10a depict the ordered and aligned pattern formation near an edge where the electrode separation distance is reduced from 193 nm (d; right half of the images in Figures 9a and 10a) to 150 nm (d_h; left half). Variation of distance causes an additional sharp spatial gradient of electrostatic conjoining pressure, ϕ_{EL}, across the edge. The flow of liquid from higher (less negative) electric potential, ϕ_{EL}, to lower ϕ_{EL} causes a localized cylindrical-line elevation adjacent to the heterogeneous edge and parallel to it (first image of Figure 10). For thinner films, the line elevation disintegrates at early times into columns due to the e-field induced instability assisted by a locally high curvature of cylindrical thread (image 1 of Figure 9a and b). For thicker films where the threads are of lower curvature, it takes much longer to develop undulations of the thread that
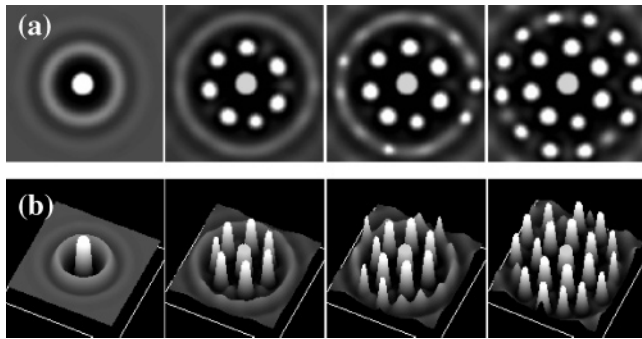
Figure 11. (a) Spatiotemporal evolution of a 25 nm thick film on a $5\lambda_m \times 5\lambda_m$ domain, where λ_m is the characteristic length scale based on the surroundings of the patch. The top electrode pattern consists of a central circular patch/groove, where the electrode spacing is at a minimum, $d_h = 80$ nm. In the remaining part, $d = 100$ nm. The nondimensional times for images 1–4 are $T = 442\,575$, $807\,493$, $911\,032$, and $164\,985$, respectively. (b) 3D surface profiles of the images in part a.

Figure 12. (a) Spatiotemporal evolution of a 75 nm thick film on a $5\lambda_m \times 5\lambda_m$ domain, where λ_m is the characteristic length scale based on the surroundings. The top electrode pattern consists of a central circular patch, where the electrode spacing is at a minimum, $d_h = 80$ nm. In the remaining part, $d = 100$ nm. The nondimensional times for images 1–4 are $T = 1.4$, 69.2, 83.0, and 121.9, respectively. (b) 3D surface profiles of the images in part a.

appears intact rather than fragmented into distinct columns ($h_0 = 93$ nm, $\xi = 0.61$; Figure 10). The alignment of the pattern brought about by the edge is limited to two to three adjacent rows of liquid columns or parallel threads. Interestingly, for lower mean film thickness ($h_0 = 50$ nm) and higher ξ (=2 based on $d_h = 150$ nm), the isolated columns formed are separated by an average distance of $\sim\lambda_m$, within the same row (images 1 and 2 of Figure 9). The formation of the subsequent new row or line of columns adjacent to the previous row continues until the more random e-field patterns start to evolve on the remaining part of the substrate, as seen for a uniform electric field. Thus, for thinner films (Figure 9), the structure away from the edge is nearly hexagonal, whereas, for thicker films (Figure 10), it is randomly oriented in the last image of Figure 10a. As discussed earlier, this random pattern results from a rapid coalescence of columns (image 3 of Figure 10a). Finally, there are no patterns seen on the right side of the electrode in these simulations because of the much larger time scale for instability there due to higher gap distance.

Thus, a locally controlled ordering and alignment of patterns is possible by the presence of an edge on the electrode. However, this control is limited to distances of $\sim(2-3)\lambda_m$ from the edge. This provides a simple thumb rule for the formation of ordered structures by an electrode patterned as parallel stripes of protruded regions. The width of such stripes (edge-to-edge distance) should not exceed $\sim5\lambda_m$ to obtain alignment of patterns in the intervening space.

In summary, the simulated structures near the edge of an electrode consist of a couple of parallel lines of liquid columns or long cylindrical ridges coexisting with hexagonally arranged columns or randomly oriented short ridges away from the edge. These structures are indeed in full accord with and explain the experimentally observed structures near the edge of an electrode.[26-32]

3.2.2. Heterogeneity II: Circular Elevation. Figures 11 and 12 depict the formation of ordered liquid columns and circular ridges around a circular elevation of the electrode, where the electrode spacing is lower than its surroundings. This causes a higher electric field at the location of the patch and a sharp spatial gradient of the electrostatic conjoining pressure, ϕ_{EL}, across the edge of the circular patch. As in the case of a straight edge, the resulting flow causes depletion of liquid just outside of the patch periphery and an elevated ring of liquid ridge surrounding it. A central column underneath the patch
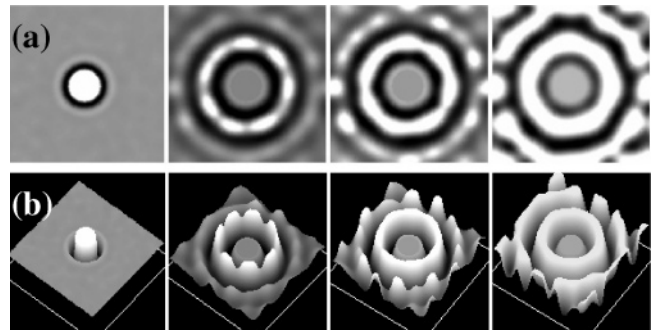
is formed immediately (the first images in Figures 11 and 12). A circular liquid ridge around the patch is caused largely by the radially inward flow, which causes another depression surrounding the ridge on the outside. For thinner films (Figure 11), the liquid ridge depletes the supply of liquid and has a higher curvature. Such a ridge fragments into circular columns before its attachment to the top electrode because of the e-field instability assisted by its cross-sectional curvature. Thus, isolated secondary ordered columns are formed from the primary annular elevation (image 2 of Figure 11) and the same process repeats radially outward (images 3 and 4). The average distance between two columns is found close to the characteristic length scale of the instability in the patch surroundings, λ_m. On the basis of a large number of simulations, it could be verified that the number of secondary columns formed around a patch increases with increasing size of heterogeneous patch as the intercolumn distance always remains close to λ_m. An increase in the volume fraction of liquid in the gap ($\xi = 0.33$) leads to the formation of a continuous ridge around the patch rather than isolated columns (Figure 12), as in the case of a straight edge discussed earlier. There is some initial tendency for the formation of columns (image 2 of Figure 12) when the liquid volume and curvature are low. However, increased and continued liquid supply leads to the coalescence of these rudimentary columns until a thick annular ring attached to the top electrode forms (images 3 and 4). However, the second-generation ring subsequently formed around the primary ring has a greater tendency for disintegration in isolated columns. The radially outward propagation of ordered structures continues until the appearance of instability in the surroundings. The distance between two annular ripples is still found to be close to λ_m.

Locally ordered patterns with a column spacing close to λ_m and identical to those reported here were indeed seen in experiments[26,27] and were thought to result from the local heterogeneities of the electric field, caused, for example, by the presence of a foreign particle.

In summary, an additional gradient in electrostatic force due to step heterogeneity of the electric field causes faster instability and ordered pattern formation. The volume fraction of the liquid in the gap has a critical role in determining the quasi-steady mesostructures that are eventually formed.

3.2.3. Heterogeneity III: Periodic Variation of Electrode Height and Electric Field. In this section, we discuss the effect of continuous periodic patterning of the top electrode
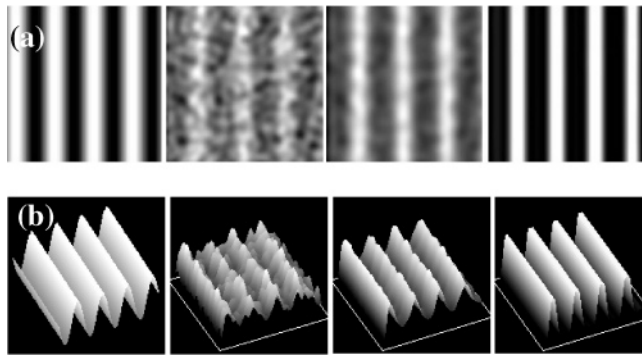
Figure 13. (a) Evolution of a 50 nm thick film in the presence of a periodically varying electric field on a $4\lambda_m \times 4\lambda_m$ domain, where λ_m is the characteristic length scale based on d_{avg}. The first image shows the top electrode pattern having a sinusoidal pattern of $d_{avg} = 100$ nm, fr = 1 ($L_p = \lambda_m$), and $\epsilon_h = 0.1$. The nondimensional times of evolution for images 2−4 are $T = 6$, 17, and 1486, respectively. (b) 3D surface profiles of the images in part a. Black represents the minimum thickness, and white represents the maximum thickness. The last film pattern is 180° out of phase with the electrode pattern (image 1), implying maximum film thickness below the protruding part of the top electrode.

on the microfluidic structure formation. Continuous periodic sinusoidal variation of the position of the upper electrode is introduced by $d = d_{avg} + \epsilon_h \sin(2\pi x/L_p)$, where d_{avg} is the mean separation distance between the two electrodes, ϵ_h is the amplitude of distance variation, and L_p is the pattern periodicity expressed as $L_p = \lambda_m \times$ fr. Here, λ_m is the mean characteristic length scale of the instability based on d_{avg} and the fraction parameter, fr, of order 1 is the regime of interest where the heterogeneity length scale competes with the basic instability length scale, $L_p \sim \lambda_m$. We have thus considered fr in the range 0.5−2. As may be expected, the cases when $L_p \gg \lambda_m$ or $L_p \ll \lambda_m$ are not interesting from the viewpoint of ideal templating of the electrode pattern in the film. In both of these cases, the film pattern loses synchronization with the electrode pattern (results not shown), as has also been shown to be the case in the dewetting on physiochemically patterned substrates.[43−51] Basically, if $L_p \gg \lambda_m$, the film pattern under the electrode protrusions resembles that under a flat electrode. In the opposite case of $L_p \ll \lambda_m$, the film pattern develops a large number of defects and every protrusion of the electrode cannot produce a liquid column because of a large surface energy penalty for deformation on small scales. Both of the above effects will become clear in the discussions below related to the extreme cases considered, namely, fr = 2 and 0.5, corresponding to $L_p = 2\lambda_m$ and $L_p = \lambda_m/2$, respectively.

On the basis of a large number of simulations, it was observed that the thin film morphology in the presence of a spatially periodic electric field crucially depends on the periodicity ($L_p = $ fr $\times \lambda_m$) and the amplitude, ϵ_h, of the top electrode pattern (Figures 13−17). However, regardless of the pattern periodicity and its amplitude, the initial structure always organizes on a length scale close to the pattern periodicity, L_p (image 2 of Figures 13−17). However, later stages of evolution are governed by L_p and ϵ_h as well as by the characteristic instability length scale based on the *minimum separation distance* between the two electrodes, namely, $\lambda_{m-d_{min}}$, evaluated at the minimum electrode separation distance, $d_{min} = d_{avg} - \epsilon_h$. This is the location of the strongest electric field.

Figures 13−17 depict the effect of pattern periodicity on thin film structure formation. For $L_p \sim \lambda_m$, parallel cylindrical ridges are formed under each protrusion of
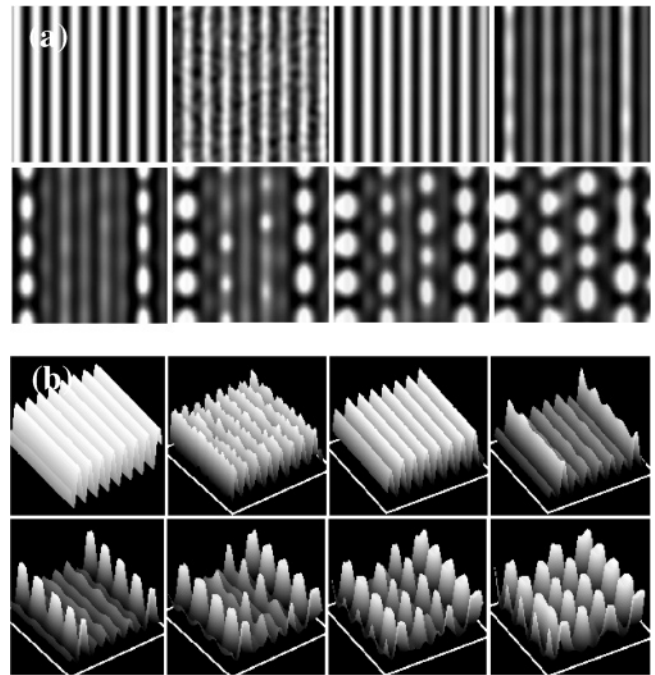

Figure 14. (a) Evolution of a 50 nm thick film in the presence of a periodically varying electric field on a $4\lambda_m \times 4\lambda_m$ domain, where λ_m is the characteristic length scale based on d_{avg}. The first image shows the top electrode pattern with the following specifications: $d_{avg} = 100$ nm, fr = 0.5 ($L_p = 0.5\lambda_m$), and $\epsilon_h = 0.1$. Black represents the minimum thickness, and white represents the maximum thickness. The nondimensional times of evolution for images 2−8 are $T = 5$, 171, 1916, 2443, 2935, 3228, and 3719, respectively. (b) 3D surface profiles of the images in part a.
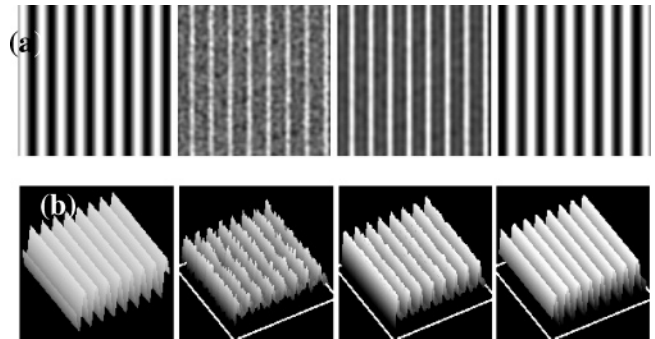

Figure 15. (a) Evolution of a 50 nm thick film in the presence of a periodically varying electric field on a $4\lambda_m \times 4\lambda_m$ domain, where λ_m is the characteristic length scale based on d_{avg}. The first image shows the top electrode pattern with the following specifications: $d_{avg} = 100$ nm, fr = 0.5 ($L_p = 0.5\lambda_m$), and $\epsilon_h = 0.4$. Black represents the minimum thickness, and white represents the maximum thickness. The nondimensional times of evolution for images 2−4 are $T = 0.6$, 2.5, and 560, respectively. (b) 3D surface profiles of the images in part a.

the top electrode (images 2−4 of Figure 13) where the electric field is maximum. The thin film dewets the bottom flat electrode at the positions of the valleys of the top electrode (image 4 of Figure 13). Thus, an ideal 180° out-of-phase templating of the top electrode pattern is obtained at the thin film interface. The resulting liquid microstructure is actually quasi-stable over long times but would ripen over very long times due to slight imbalances of the Laplace pressure, since not all ridges remain exactly identical. However, the quasi-stable pattern can be quenched or cross-linked to make it permanent. A large number of 2D and 3D simulations verified that, for $L_p = $
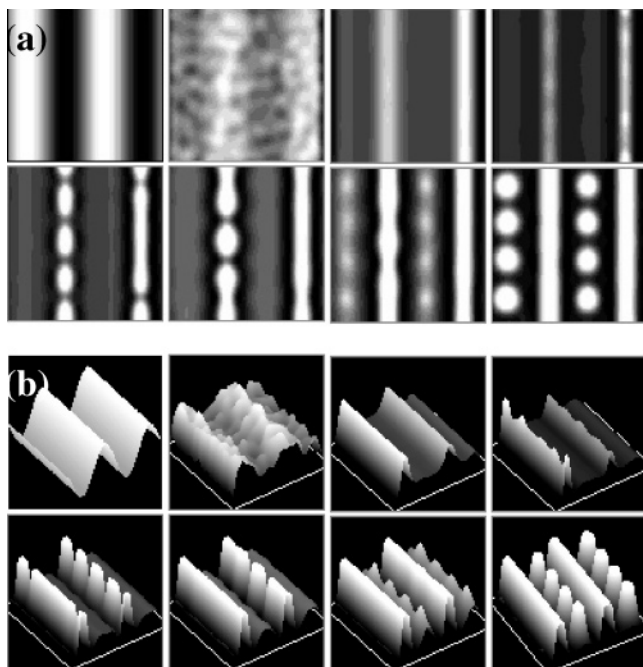
Figure 16. (a) Evolution of a 50 nm thick film subjected to a periodically varying electric field on a $4\lambda_m \times 4\lambda_m$ domain, where λ_m is the characteristic length scale based on d_{avg}. The first image shows the top electrode pattern with the following specifications: $d_{avg} = 100$ nm, fr $= 2$ ($L_p = 2\lambda_m$), and $\epsilon_h = 0.1$. The nondimensional times of evolution for images 2−8 are $T = 36, 134, 1673, 2001, 2619, 3486,$ and 5057, respectively. (b) 3D surface profiles of the images in part a.
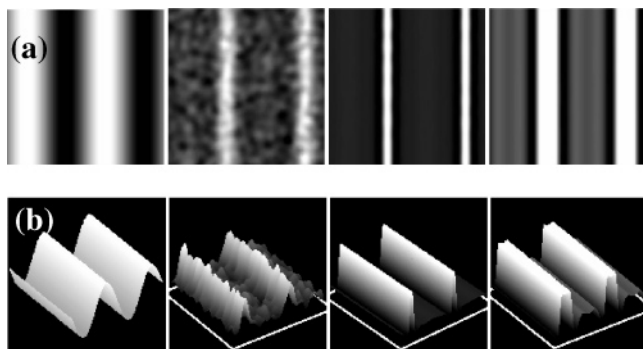

Figure 17. (a) Evolution of a 50 nm thick film subjected to a periodically varying electric field on a $4\lambda_m \times 4\lambda_m$ domain, where λ_m is the characteristic length scale based on d_{avg}. The first image shows the top electrode pattern with the following specifications: $d_{avg} = 100$ nm, fr $= 2$ ($L_p = 2\lambda_m$), and $\epsilon_h = 0.4$. The nondimensional times of evolution for images 2−4 are $T = 7, 163,$ and 1054, respectively. (b) 3D surface profiles of the images in part a.

λ_m, the thin film pattern ideally templates the inverse top electrode pattern irrespective of the value of ϵ_h.

For $L_p < \lambda_m$, it is observed that the final morphology depends on the amplitude, ϵ_h, of the top electrode pattern (Figures 14 and 15). The initial evolution always follows the top electrode pattern, and elevated liquid stripes are formed directly underneath all the protrusions of the top electrode (images 2 and 3 of Figures 14 and 15). For smaller amplitudes ($\epsilon_h = 0.1$) such that $L_p < \lambda_{m-d_{min}}$, the interridge distance is close to $L_p = \lambda_m/2$. However, a further reorganization of the initial ridges occurs to eliminate some ridges and form more prominent ridges/row of columns with a periodicity closer to λ_m. Further, the ridges break into isolated columns (images 6−8 of Figure 14). The intercolumn distance for the columns belonging to the same row is also close to λ_m. An interesting find is thus

that the mean linear theory length scale is respected for a small-amplitude heterogeneity. Since the spacing between the protruded portions of the top electrode is less than λ_m, not all of these domains remain "live" in creating liquid elevations underneath them. At the later stages of evolution, ripening and coalescence between adjacent columns can also occur (image 8 of Figure 14).

In contrast to the above, the top electrode with a larger amplitude of the sinusoidal pattern ($\epsilon_h = 0.4$, $L_p > \lambda_{m-d_{min}}$) having the same periodicity, $L_p = \lambda_m/2$, induces an ordered thin film pattern (Figure 15) replicating the top electrode. Alternating liquid cylinders and depressions are formed along the positions of the trough and crest of the top electrode, resulting in a nearly perfect templating. Thus, the condition for ideal templating can be generalized on the basis of these results. It was indeed verified that an ideal replication of the electrode pattern becomes possible only when the amplitude and periodicity are such that $L_p \geq \lambda_{m-d_{min}}$. This becomes possible by increasing the amplitude of electrode heterogeneity so that the linear theory results for a uniform field are no longer valid.

When the electrode pattern periodicity is larger than λ_m ($L_p > \lambda_m$), the initial evolution still leads to the formation of liquid ridges commensurate with the electrode periodicity (images 2−6 of Figure 16; images 2 and 3 of Figure 17). For smaller amplitude patterns ($\epsilon_h \leq 0.1$), secondary structures (isolated columns or drops) are then formed between the two primary parallel ridges (images 7 and 8 of Figure 16). The fragmented secondary structure arises because of the depletion of liquid in the formation of primary continuous ridges. The distance between the two consecutive rows and the distance between the two columns on the same line are both close to λ_m. Thus, for small heterogeneities of the field, the eventual structure length scale is again close to the mean spinodal length scale, λ_m, notwithstanding a larger separation ($=2\lambda_m$) between the protrusions of the electrode.

For a large-amplitude heterogeneity, $\epsilon_h = 0.4$, the secondary column formation is entirely suppressed and the thin film pattern ideally replicates the electrode pattern (image 4 of Figure 17). A much higher localized electric field in this case widens the primary linear ridges by transporting more liquid from the surroundings, where the field is much weaker. In such a case, the effect of flow caused by the imposed gradient of the field wins over the action of the uniform field in causing the instability on the length scale of λ_m. Thus, the formation of secondary structures that respect λ_m scaling is entirely suppressed.

In summary, a large number of simulations revealed (not all of which are shown here) that an ideal replication of the top electrode pattern in a thin film occurs when $\lambda_m \geq L_p \geq \lambda_{m-d_{min}}$, where $\lambda_{m-d_{min}}$ is the length scale based on the minimum separation distance of electrodes. For systems with $L_p > \lambda_m$, ideal templating is obtained only for large amplitudes, $\epsilon_h > 0.2$, which suppresses the formation of secondary structures that are out of sync with the electrode pattern. Clearly, these results have important implications in terms of designing the electrode patterns for the engineering of desired ordered structures in thin films of soft materials. Basically, it is possible to increase the density of thin film patterns (reduce spacing below λ_m) by imposing strong gradients or large amplitudes in the top electrode. This strategy makes the flow resulting from the *imposed e-field gradient* dominate over the flow from the e-field variations that are caused by the local thickness variations (spinodal instability). The latter produces the structure length scales of the order λ_m, whereas the former encourages organization on the length scale of the electrode pattern.
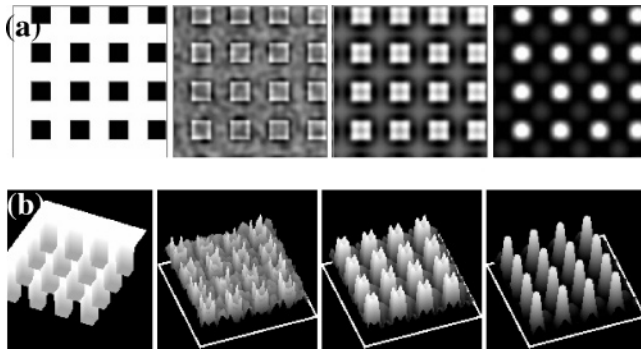
Figure 18. (a) Spatiotemporal evolution of a 50 nm thick film in the presence of a block patterned top electrode on a $4\lambda_m \times 4\lambda_m$ domain, where λ_m is the characteristic length scale based on d_{avg}. The first image shows the top electrode pattern with the following specifications: $d_{min} = 95$ nm (electrode separation distance at block), $d_{max} = 100$ nm, and fr = 1 ($L_{px} = L_{py} = \lambda_m$). The nondimensional times of evolution for images 2−4 are $T = 3$, 41, and 548, respectively. (b) 3D surface profiles of the images in part a.

3.2.4. Heterogeneity IV: Block Patterns. In this section, we study the effect of a more complex, 2D template geometry with confinements in both the x and y directions. The block patterned top electrode consists of arrays of rectangular protrusions. Such an electrode induces spatially varying e-field and sharp gradients along the boundary of the protrusions. The separation distance between the two electrodes is the minimum (maximum), and the electric field is the maximum (minimum) at the position of the protrusions (surrounding channels). Simulations predict that the evolution and the final morphology of thin liquid film crucially depend on the pattern periodicity and height of the blocks (Figures 18−21). An ideal replication of the geometry of the upper electrode should result in periodic arrays of liquid columns (for example, image 8 of Figures 18 and 20), that may be used as masks, sacrificial layers, sensors, and synthetic media for separation processes and in a variety of optoelectronic devices and processes.

Figures 18−21 depict the effect of top electrode pattern periodicity and height of blocks on the thin film evolution. Regardless of the pattern periodicity, initial random perturbations spontaneously reorganize on a length scale close to the pattern periodicity (image 2 of Figures 18−21). The systems in which the top electrode pattern periodicity ($L_{px} = L_{py}$) equals the characteristic length scale, λ_m, the pattern formed at the later stage of evolution ideally replicates the top electrode pattern (image 4 of Figure 18). In essence, the spatial scale of the imposed e-field variations matches that resulting from the thickness variations or the spinodal length scale. Templating is always ideal under this situation. The evolution proceeds with the formation of pillars of more nearly square cross section, and the four corners of each pillar reach the top electrode (images 2 and 3 of Figure 18). At longer times, the columns of increasingly circular cross section emerge to minimize the surface energy (image 4 of Figure 18).

In contrast, if the electrode pattern periodicity is smaller than both λ_m and $\lambda_{m-d_{min}}$ (for example, $L_{px} = L_{py} = 0.5\lambda_m < \lambda_{m-d_{min}}$ in Figure 19), the initially formed large number of liquid elevations eventually resolve in a smaller number of columns that are separated by the spinodal characteristic length scale, λ_m (image 7 of Figure 19). Thus, some of the electrode protrusions become ineffective in organizing the structure on the scale of electrode pattern. The resulting pattern periodicity is larger than the electrode pattern. At a still later stage of evolution, coalescence
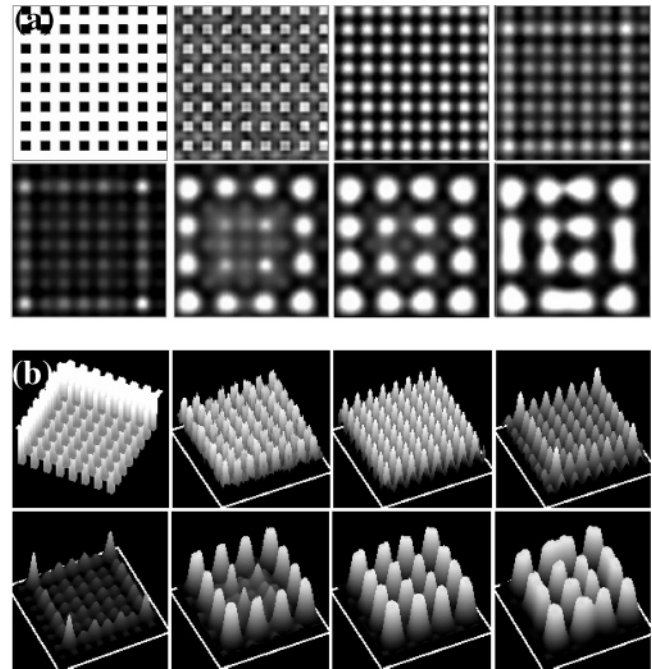

Figure 19. (a) Spatiotemporal evolution of a 50 nm thick film in the presence of a block patterned top electrode on a $4\lambda_m \times 4\lambda_m$ domain, where λ_m is the characteristic length scale based on d_{avg}. The first image shows the top electrode pattern with the following specifications: $d_{min} = 95$ nm (electrode separation distance at block), $d_{max} = 100$ nm, and fr = 0.5 ($L_{px} = L_{py} = 0.5\lambda_m$). The nondimensional times of evolution for images 2−8 are $T = 3$, 120, 1637, 2150, 3037, 3567, and 4319, respectively. (b) 3D surface profiles of the images in part a.
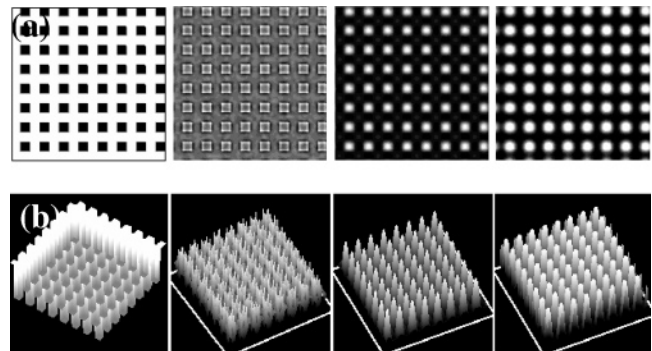

Figure 20. (a) Spatiotemporal evolution of a 25 nm thick film in the presence of a block patterned top electrode on a $4\lambda_m \times 4\lambda_m$ domain, where λ_m is the characteristic length scale based on d_{avg}. The first image shows the top electrode pattern with the following specifications: $d_{min} = 70$ nm (electrode separation distance at block), $d_{max} = 100$ nm, and fr = 0.5 ($L_{px} = L_{py} = 0.5\lambda_m$). The nondimensional times of evolution for images 2−4 are $T = 18$, 2329, and 15 808, respectively. (b) 3D surface profiles of the images in part a.

also starts (image 8 of Figure 19). However, by increasing the height of the protrusions further, such that the characteristic length scale based on the minimum separation distance, d_{min} ($\lambda_{m-d_{min}}$), exceeds the pattern periodicity, more ideal templating can be obtained (results not shown). This is similar to the effect discussed in Figure 15 where a stronger imposed e-field gradient can overwhelm the spinodal effects. For the same top electrode pattern, ideal templating can also be obtained by changing the film thickness so that the condition for the ideal templating is satisfied. For example, Figure 20 depicts the evolution of a 25 nm thick film where the top electrode is block patterned with a minimum separation distance of 70 nm. In this case, the electrode pattern periodicity is
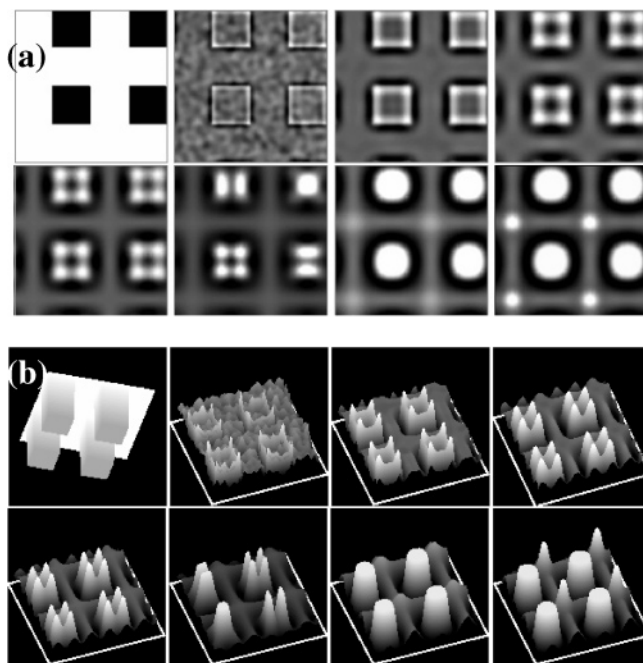
Figure 21. (a) Spatiotemporal evolution of a 50 nm thick film in the presence of a block patterned top electrode on a $4\lambda_m \times 4\lambda_m$ domain, where λ_m is the characteristic length scale based on d_{avg}. The first image shows the top electrode pattern with the following specifications: $d_{min} = 95$ nm (electrode separation distance at block), $d_{max} = 100$ nm, and fr = 2 ($L_{px} = L_{py} = 2\lambda_m$). The nondimensional times of evolution for images 2−8 are T = 3, 46, 256, 661, 1014, 1650, and 1868, respectively. (b) 3D surface profiles of the images in part a.

greater than $\lambda_{m-d_{min}}$. The thin film pattern thus almost ideally replicates the electrode pattern (image 4 of Figure 20). From these and many other simulations (not shown), we can generalize the condition for ideal templating as $\lambda_m \geq (L_{px} = L_{py}) \geq \lambda_{m-d_{min}}$. It may be reiterated that λ_m depends on the film thickness and the mean separation distance between the electrodes, whereas $\lambda_{m-d_{min}}$ is modulated by the amplitude of the imposed e-field variation.

Finally, an interesting case of evolution for $L_{px} = L_{py} > \lambda_m$ is shown in Figure 21. The homogeneous e-field instability underneath the electrode protrusions is relatively weak compared with the imposed e-field gradient driven flow emanating at the corners. The liquid underneath the block edges thus first jumps in contact producing hollow pillars or columns of nearly rectangular visage (images 2 and 3 of Figure 21). Each primary hollow column then splits into four corner pillars (images 4 and 5), which grow in size by the further addition of liquid (image 6) and eventually coalesce into a single circular pillar under each protrusion (image 7). Finally, the excess liquid at the center line of the "corridors" or the channels is transformed into secondary slender columns (image 8). These secondary structures have the same genesis as discussed in the context of a small-amplitude periodically varying electric field where spinodal effects become important at later times. Again, as discussed earlier, the formation of these secondary structures can be suppressed by increasing the gradient of applied e-field by increasing the height of the protrusions. This leads to a more ideal templating of the electrode pattern (results not shown).

4. Conclusions

We have presented a theoretical study of electric field induced instabilities and pattern formation in thin liquid films confined between two electrodes with an air gap between the film surface and the top electrode. On the basis of 3D simulations for a homogeneous electric field, conditions for a morphological phase inversion from liquid columns to holes have been investigated. For lower volume fractions ($\varphi < 0.25$) of the liquid in the gap, a nearly hexagonal ordering of quasi-stable circular columns (liquid-in-air dispersion) occurs. Upon increasing the volume fraction, hexagonal ordering becomes increasingly distorted and columns acquire elliptical and then more complex cross sections such as randomly oriented long ridges. For a very high value of volume fraction of $\varphi \geq 0.75$, a rapid coalescence of these ridgelike columns causes a *phase inversion*, leading to the formation of holes of air entrapped in liquid matrix (air-in-liquid dispersion).

A greater variety of ordered structures can be produced by employing a patterned electrode that produces a lateral variation and gradient of the electric field and causes a directed movement of the liquid toward the higher intensity of the field. Competition between the applied gradient driven flow and the spinodal flow engendered by the gradients generated by the thickness variations determines the morphology. By applying a step change of electric field across an edge, lines of columns separated by λ_m distance form starting from the edge. This ordered arrangement of columns in lines resolves into homogeneous spinodal patterns beyond $\sim3\lambda_m$ distance from the edge. Thus, a simple thumb rule for the creation of ordered complex patterns would be to have any two edges in a template to be no more than $\sim4\lambda_m$ apart. Similarly, instabilities initiated by a circular protrusion of the top electrode engender a central circular column surrounded by a ring or two of satellite columns separated by nearly λ_m. As in the case of a homogeneous substrate and an edge, increasing the volume fraction of liquid leads to the formation of long continuous ridges of cylindrical cross section, rather than isolated columns. In the case of a circular patch, this leads to a ripplelike peripheral structure.

An important question addressed here concerns the conditions under which the electrode pattern can be faithfully replicated in the film. The conditions for ideal templating are explored with the help of two basic patterns—stripes and blocks, from which many useful generalizations also emerge for more complex periodic patterns. Simulations show ideal templating occurs when the pattern periodicity slightly exceeds the spinodal length scale evaluated on the basis of the maximum e-field strength present in the pattern, namely, $L_p \geq \lambda_{m-d_{min}}$ (characteristic length scale based on minimum separation distance of two electrodes). At the same time, the condition $L_p \leq \lambda_m$ (characteristic length scale based on mean separation distance) should also be satisfied. For $L_p > \lambda_m$ and relatively weak imposed gradients (for a small amplitude of electrode patterns), secondary structures form due to spinodal reasons at the later stages of evolution, thereby increasing the number density of thin film features beyond that of the electrode pattern. The use of a strong *gradient electrode* with deeper grooves (nondimensional amplitude of $\epsilon_h > 0.25$) suppresses the secondary structure formation, leading to almost ideal templating. The results imply that the number density of the electric field induced patterns (and also the pattern size) can be altered by tuning the mean film thickness (volume fraction of liquid), periodicity, and depth (amplitude) of the grooves on the top electrode and by varying the applied voltage. For example, for a given top electrode pattern, the number density of the columns is increased by decreasing the film thickness and by increasing the voltage. Clearly, the results have implications in elec-

trostatic lithography and in the design and interpretation of thin film experiments. For example, the above results concerning the hexagonal and disordered structures in a homogeneous e-field and locally ordered structures around an edge or spot heterogeneity have already been documented in experiments.[26–32]

LA0472100